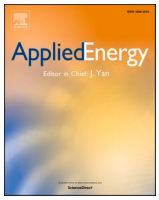
Applied Energy 427 (2027) 128942



Contents lists available at ScienceDirect

Applied Energy

journal homepage: www.elsevier.com/locate/apenergy



A novel transient zero-dimensional physics-based model of vanadium redox flow batteries with electrolyte crossover-induced capacity fade

Shaojin Wang [a], Jinrui Tang [a,*], Binyu Xiong [a,*], Yang Li [b], Changjun Xie [a], Feifei Dong [c], Xinan Zhang [d]

[a] School of Automation, Wuhan University of Technology, Wuhan 430070, China
[b] School of Electrical Engineering and Automation, Wuhan University, Wuhan 430070, China
[c] Electric Power Planning & Engineering Institute Co., Ltd, Xicheng District, Beijing 100120, China
[d] School of Engineering, University of Western Australia, Crawley, WA 6009, Australia

HIGHLIGHTS

- A dynamic model with electrolyte crossover-induced capacity fade is proposed.
- The dynamic process of vanadium ions, protons, and electrolyte volume is modeled.
- The accuracy of the model is validated via over 300-cycle aging experiments.
- Model's applicability is demonstrated through different current densities and cell sizes.
- The model achieves an improved prediction accuracy compared with state-of-art model.

ARTICLE INFO

Keywords:
Vanadium redox flow batteries (VRBs)
Dynamic model
Electrolyte crossover
Capacity loss
Volume imbalance

ABSTRACT

Conventional lumped models of vanadium redox flow batteries (VRBs) typically neglect bulk electrolyte transfer because its effects are often insignificant over short time scales. This simplification, however, prevents accurate representation of electrolyte crossover-induced volume imbalance and the associated capacity fade, limiting their applicability to performance prediction and control. This paper presents a novel transient zero-dimensional (0-D) physics-based VRB model that explicitly considers electrolyte migration mechanisms derived from first principles. The model corrects the convection term in the vanadium ion concentration equations and the pressure difference term in the electrolyte volume equations as incremental improvements, while its novel enhancement lies in capturing the dynamic behavior of proton migration during VRB operation. Osmotically driven water transport across the membrane is modeled using Schlögl's equation, and the combined effects of vanadium ion crossover, osmotic pressure, and shunt currents are integrated to quantify electrolyte volume imbalance. Experimental validation over 300 charge-discharge cycles demonstrates significantly improved prediction accuracy compared with the conventional model, achieving an average capacity prediction error of less than 2.58% and an electrolyte volume prediction error of less than 5.33%. Results indicate that osmotic pressure-driven transport is the dominant contributor to electrolyte imbalance. The model's applicability is further demonstrated under different current densities and cell sizes, providing a theoretical basis for future degradation analysis and operational guidance of VRB systems.

1. Introduction

Vanadium redox flow batteries (VRBs) have attracted increasing attention as a promising energy storage solution for integrating renewable energy into power grids, thanks to their high energy efficiency, long service life, and flexible power ratings [1,2]. However, VRBs suffer from capacity degradation during long-term operation, leading to performance deterioration, increased maintenance requirements, and reduced system reliability [3,4]. Addressing capacity degradation is therefore critical for the reliable deployment of VRBs, particularly in large-scale

* Corresponding authors.
E-mail addresses: tangjinrui@whut.edu.cn (J. Tang), bxiong2@whut.edu.cn (B. Xiong).

https://doi.org/10.1016/j.apenergy.2026.128942
Received 29 June 2026; Received in revised form 16 August 2026; Accepted 25 September 2026
0306-2619/© 2026 Elsevier Ltd. All rights are reserved, including those for text and data mining, AI training, and similar technologies.

energy applications [5,6].

As a core component of the VRB, the proton exchange membrane (PEM) is theoretically expected to allow only protons to pass through, while preventing ion exchange between the two electrodes. However, in practical operation, the membrane behaves non-ideally. The permeation abilities of vanadium ions in different valence states vary [7], leading to ion crossover between the positive and negative electrodes and consequently causing self-discharge side reactions. Meanwhile, water molecules of different volumes are carried along when ions migrate across the membrane. Over long-term operation, the continuous accumulation of ions and water induces a severe electrolyte imbalance, ultimately resulting in a marked reduction in usable capacity [8]. Previous literature has made significant contributions to elucidating the mechanisms of capacity decay and the kinetics of vanadium ion transfer. For instance, Sun et al. [9] demonstrated that the capacity decay in VRBs with Nafion 115 and VX-20 membranes is primarily attributable to vanadium ion crossover and side reactions, respectively. Song et al. [10] systematically investigated the mechanism of electrolyte volume imbalance, revealing that the difference in electrolyte viscosity is the main cause of electrolyte imbalance, and that a higher flow rate exacerbates the volume imbalance. Sun et al. [7] concluded that electrolyte imbalance in VRBs originates from ion crossover and water migration. On this basis, Loktionov et al. [11] conducted further research and quantitatively analyzed the coupling relationship between ion crossover and capacity decay based on the average oxidation state (AOS) of the electrolyte. To systematically analyze and quantify the degradation process, the numerical models of VRBs have been developed, which comprehensively incorporate water transport and electrolyte imbalance induced by electro-osmotic drag, osmotic drag, diffusion, and ion crossover [8,12–17]. Skyllas-Kazacos et al. [18,19] focused on an in-depth analysis of vanadium ion diffusion and water transport. Li et al. [20,21] employed a dynamic model to estimate membrane permeability and explore the effects of electrolyte imbalance. These studies are critical for determining the timing of electrolyte mixing and achieving capacity recovery, which directly affects system safety, service life, and economic viability.

Accurate modeling of capacity degradation mechanisms is essential for diagnosis, performance assessment, and the development of effective mitigation and control strategies. Considerable research efforts have been devoted to modeling capacity fade in VRBs based on physical principles [22,23], and existing approaches can be broadly categorized into multi-dimensional and zero-dimensional (0-D) models [24,25]. Multi-dimensional models are divided into one-, two-, or three-dimensional (1-D/2-D/3-D) categories, with spatial distribution considered within the system. They aim to resolve detailed physicochemical processes within the cell, including species transport in porous electrodes, local reaction kinetics, and potential distributions [12,26]. Although these models provide detailed insight into degradation mechanisms, their high computational complexity limits their applicability in long-term monitoring and system-level control applications [8,27].

In contrast, 0-D models describe the overall system behavior based on spatially averaged variables, focusing on global mass balance and dominant transport processes [13,28–30]. With dynamic response times of only a few seconds [31,32], they offer significantly improved computational efficiency, making them well-suited for system-level operational planning and control applications [33,34]. Consequently, 0-D models have been widely adopted to investigate capacity fading in VRBs [35]. For example, Tang et al. developed an electrochemical model based on mass balances of the four vanadium ions to predict capacity loss in VRBs [36]. The effects of side reactions and different proton exchange membranes on capacity fading were further analyzed in [37]. Pugach et al. [38] identified the crossover flux during battery cycling. To investigate the contribution of different crossover mechanisms, a 0-D dynamic model based on charge and mass conservation was proposed for a single VRB cell [39].

Nevertheless, these models mostly only offer qualitative analysis and have not yet conducted quantitative calculations or long-term operation predictions [15]. Although some studies have addressed aspects of this problem [13], none of these models fully and explicitly capture the coupled imbalance mechanism between the positive and negative electrolyte volumes. As a result, capacity fading cannot be fully explained, leading to reduced modeling accuracy and limited applicability for long-term operation in practical VRB systems. Table 1 presents a detailed comparison between the proposed model and existing models.

To overcome the aforementioned limitations and increase the physical interpretability of the model, this paper presents a novel transient 0-D physics-based model based on first principles that explicitly incorporates bulk electrolyte crossover. The main contributions of this work are summarized as follows:

1) The proposed model aims to describe the coupled dynamics of ion transport, proton migration, and water crossover, which collectively drive bulk electrolyte imbalance during long-term VRB operation. By systematically integrating diffusion- and osmotic-pressure-driven transport processes, the proposed model enables a comprehensive interpretation of capacity fading that is not captured in existing 0-D models.
2) A system-level modeling framework is introduced in which the electrochemical cell and electrolyte tanks are treated as physically distinct yet dynamically coupled subsystems. This formulation enables explicit representation of concentration gradients and electrolyte volume variation, thereby improving long-term capacity prediction compared with conventional lumped models.
3) Extensive experimental validation is conducted over long-term cycling and a wide operating range. The results quantitatively reveal the dominant role of osmotic-pressure-driven water transport in electrolyte volume imbalance and demonstrate the accuracy of the proposed model for long-term performance prediction and degradation-oriented applications.

2. Model and development

The mathematical model is developed based on mass and charge conservation. To obtain a tractable formulation suitable for long-term performance and capacity-fade analysis, the following assumptions are adopted [8,13]:

1) The positive and negative cells and tanks have identical volumes.
2) Electrolyte volume variations occur predominantly in the tanks rather than in the cell.

Table 1
Comparisons between the proposed model and existing models.

Model		Chen et al. (2019) in APEN [15]	Zou et al. (2024) in APEN [13]	Proposed model
Vanadium ion concentrations dynamic submodel (8 dimensions)	Whether?	√	√	√
	Differences at the inlet and outlet of stack and tank	×	×	√
Proton concentration dynamic submodel (4 dimensions)	Whether?	×	×	√
	Differences at the inlet and outlet of stack and tank	×	×	√
Electrolyte volume dynamic submodel (2 dimensions)	Whether?	×	√	√
	Hydraulic pressure difference	×	×	√

3) Gas-evolving side reactions have negligible impacts on electrolyte imbalance and capacity evolution.
4) Initial conditions are perfectly known.

It should be noted that the density and viscosity of vanadium electrolytes may vary with electrolyte composition, oxidation state, and temperature. Recent measurements reported by Prieto-Díaz et al. [40] demonstrated significant variations in these properties during battery operation. In the present study, concentration-dependent property variations are not explicitly modeled. Instead, the viscosity of water and the initial electrolyte density are employed as effective reference values for transport calculations.

2.1. General description

The electrochemical reactions occurring in the VRB during the operation are summarized. Main reactions in the positive and negatives electrode are described by

$$VO^{2+} + H_2O \underset{\text{discharge}}{\overset{\text{charge}}{\rightleftharpoons}} VO_2^+ + 2H^+ + e^- \tag{1}$$

$$V^{3+} + e^- \underset{\text{charge}}{\overset{\text{discharge}}{\rightleftharpoons}} V^{2+} \tag{2}$$

Side reactions in the negative electrolyte include

$$\boldsymbol{V^{2+} + VO^{2+} + 2H^+ \rightarrow 2V^{3+} + H_2O} \tag{3}$$

$$\boldsymbol{V^{3+} + VO_2^+ \rightarrow 2VO^{2+}} \tag{4}$$

$$\boldsymbol{2V^{2+} + VO_2^+ + 4H^+ \rightarrow 3V^{3+} + 2H_2O} \tag{5}$$

Side reactions in the positive electrolyte consist of

$$\boldsymbol{2VO_2^+ + V^{2+} + 2H^+ \rightarrow 3VO^{2+} + H_2O} \tag{6}$$

$$\boldsymbol{VO_2^+ + V^{3+} \rightarrow 2VO^{2+}} \tag{7}$$

$$\boldsymbol{VO^{2+} + V^{2+} + 2H^+ \rightarrow 2V^{3+} + H_2O} \tag{8}$$

A schematic illustration of bulk electrolyte crossover in VRBs is shown in Fig. 1. The electrolyte crossover process is categorized into three distinct components: ion crossover, proton transfer, and water molecule migration. The first is driven by diffusion, while the second is driven by electro-osmosis and establishes a concentration gradient across the membrane. The combined two effect drives water molecule migration via osmosis pressure.

Fig. 2 summarizes the fading dominant causes, physicochemical mechanisms, and associated modes. In the present study, the capacity decline is primarily attributed to electrolyte imbalance induced by vanadium ion crossover, proton transport, and water migration across the membrane. Specifically, ion crossover changes the vanadium ion concentration distribution between the positive and negative electrolytes, while water migration driven by osmotic pressure and electro-osmotic drag causes electrolyte volume imbalance. These coupled transport processes gradually reduce the amount of electrochemically accessible active species, thereby leading to a decrease in the usable battery capacity.

Based on previous experimental and modeling studies [8,13], electrolyte imbalance is considered one of the dominant mechanisms responsible for long-term capacity decay in VRB systems. It should be noted that VRB capacity fading is a multifactorial process involving electrolyte-, membrane-, and electrode-related degradation mechanisms, as well as environmental and operational conditions. The present study mainly focuses on crossover- and imbalance-induced capacity decay.

As illustrated in Fig. 1, the ion concentrations at the inlet and outlet

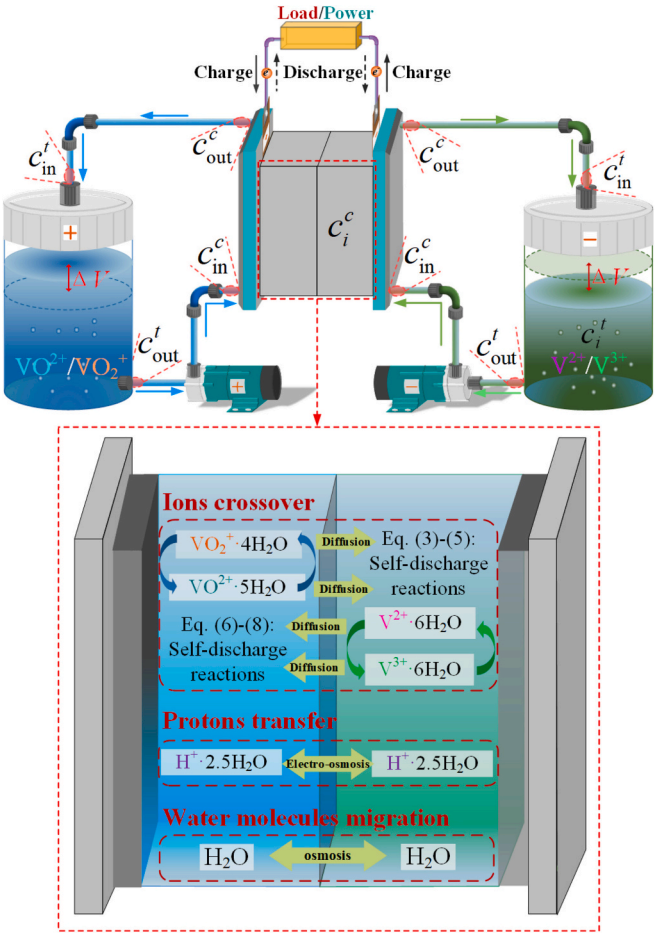


Fig. 1. Schematic of bulk electrolyte crossover of a VRB.

differ due to electrochemical reactions in the cell. To simplify the analysis, we assume that the ion concentrations in the cell are the average of the concentrations at the cell inlet and outlet. This gives

$$\begin{cases} c_i^c = \dfrac{c_{\text{in}}^c + c_{\text{out}}^c}{2} \\ c_i^t = c_{\text{in}}^c \end{cases} \tag{9}$$

where c_{in}^c and c_{out}^c denote the inlet and outlet ion concentrations of the cell in (mol/m^3), respectively. c_i^c and c_i^t denote ion concentrations in the cell and tank in (mol/m^3), respectively, where i is the valence ($i = 2, 3, 4$, and 5).

In the work, the volume of the electrolyte flow pipe is insignificant and therefore ignored. The ion concentrations at the outlet and inlet of the cell and tanks are defined as:

$$\begin{cases} c_{\text{in}}^c = c_{\text{out}}^t \\ c_{\text{out}}^c = c_{\text{in}}^t \end{cases} \tag{10}$$

where c_{in}^t and c_{out}^t denote the inlet and outlet electrolyte concentrations of the tank in (mol/m^3), respectively.

2.2. Vanadium ion concentrations dynamic submodel

Compared to the conventional models, differences at the inlet and outlet of the cell and tank are considered in this section. Accordingly, the electrolyte convection term in the submodel is modified to reflect this spatial variation.

According to (9), the cell concentrations of inlet c_{in}^c and outlet c_{out}^c are

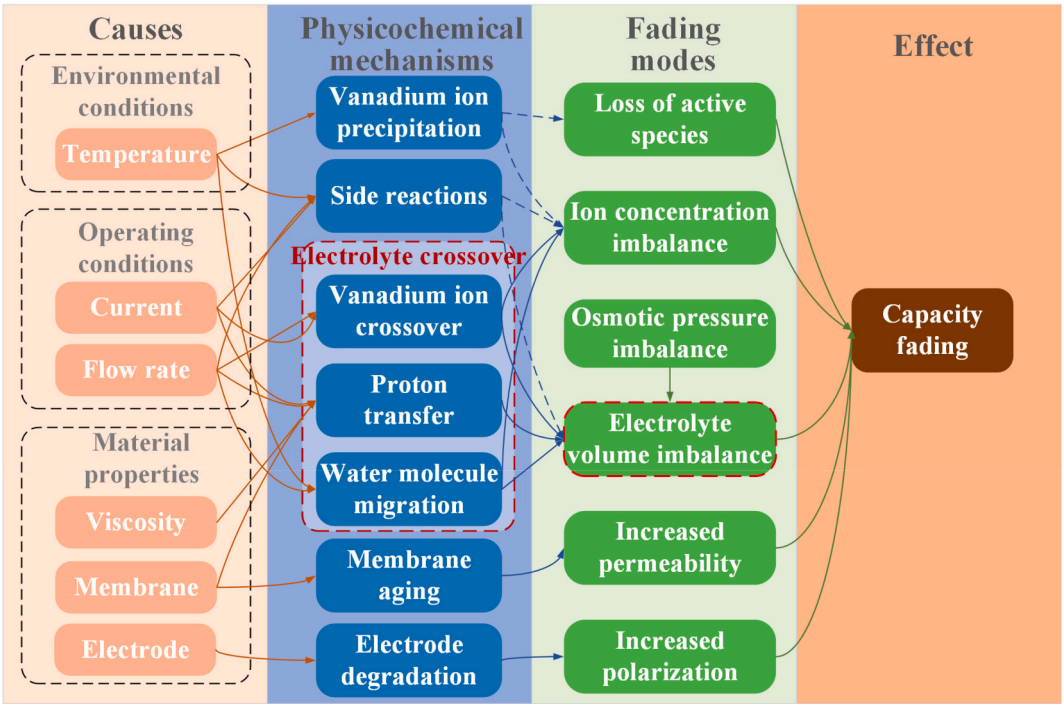


Fig. 2. Hierarchical relationship among the influencing causes, physicochemical mechanisms, and fading modes associated with VRB capacity fading.

expressed as

$$\begin{cases} c_{\text{in}}^{c} = c_i^{t} \\ c_{\text{out}}^{c} = 2c_i^{c} - c_i^{t} \end{cases} \tag{11}$$

According to (10), the tank concentrations of inlet c_{in}^{t} and outlet c_{out}^{t} can be expressed as

$$\begin{cases} c_{\text{in}}^{t} = 2c_i^{c} - c_i^{t} \\ c_{\text{out}}^{t} = c_i^{t} \end{cases} \tag{12}$$

Within a short duration Δt, the forced convection of the electrolyte results in concentration variations in the cell and tank, governed by

$$\begin{cases} \Delta c_i^{c} V_{hc} = Q\left(c_{\text{in}}^{c} - c_{\text{out}}^{c}\right)\Delta t \\ \Delta c_i^{t} V_t = Q\left(c_{\text{in}}^{t} - c_{\text{out}}^{t}\right)\Delta t \end{cases} \tag{13}$$

where V_{hc} and V_t denote the volume of the half-cell and tank in (m^3), respectively.

Substituting (11) and (12) into (13) yields the concentration of vanadium ions in the electrolyte convection term corrected in the cell and tank, i.e.,

$$\begin{cases} \Delta c_i^{c} V_{\text{hc}} = 2Q\left(c_i^{t} - c_i^{c}\right)\Delta t \\ \Delta c_i^{t} V_t = 2Q\left(c_i^{c} - c_i^{t}\right)\Delta t \end{cases} \tag{14}$$

By considering the effects of the main reactions, crossover and side reactions, shunt current, and convection, the concentrations of four vanadium ions in the cell can be described by:

$$V_{\text{hc}}\frac{\mathrm{d}c_2^{c}}{\mathrm{d}t} = \underbrace{\left(-\frac{k_2 c_2^{c}}{d} - \frac{k_4 c_4^{c}}{d} - \frac{2k_5 c_5^{c}}{d}\right) S_M}_{\text{crossover,side reactions}} + \underbrace{\frac{NJS_E}{zF}}_{\text{main reactions}} - \underbrace{\frac{I_{\text{shunt}}}{zF}}_{\text{shunt current}} + \underbrace{2Q_n\left(c_2^{t} - c_2^{c}\right)}_{\text{convection}} \tag{15}$$

$$V_{\text{hc}}\frac{\mathrm{d}c_3^{c}}{\mathrm{d}t} = \underbrace{\left(-\frac{k_3 c_3^{c}}{d} + \frac{3k_5 c_5^{c}}{d} + \frac{2k_4 c_4^{c}}{d}\right) S_M}_{\text{crossover,side reactions}} - \underbrace{\frac{NJS_E}{zF}}_{\text{main reactions}} + \underbrace{\frac{I_{\text{shunt}}}{zF}}_{\text{shunt current}} + \underbrace{2Q_n\left(c_3^{t} - c_3^{c}\right)}_{\text{convection}} \tag{16}$$

$$V_{\text{hc}}\frac{\mathrm{d}c_4^{c}}{\mathrm{d}t} = \underbrace{\left(-\frac{k_4 c_4^{c}}{d} + \frac{3k_2 c_2^{c}}{d} + \frac{2k_3 c_3^{c}}{d}\right) S_M}_{\text{crossover,side reactions}} - \underbrace{\frac{NJS_E}{zF}}_{\text{main reactions}} + \underbrace{\frac{I_{\text{shunt}}}{zF}}_{\text{shunt current}} + \underbrace{2Q_p\left(c_4^{t} - c_4^{c}\right)}_{\text{convection}} \tag{17}$$

$$V_{\text{hc}}\frac{\mathrm{d}c_5^{c}}{\mathrm{d}t} = \underbrace{\left(-\frac{k_5 c_5^{c}}{d} - \frac{2k_2 c_2^{c}}{d} - \frac{k_3 c_3^{c}}{d}\right) S_M}_{\text{crossover,side reactions}} + \underbrace{\frac{NJS_E}{zF}}_{\text{main reactions}} - \underbrace{\frac{I_{\text{shunt}}}{zF}}_{\text{shunt current}} + \underbrace{2Q_p\left(c_5^{t} - c_5^{c}\right)}_{\text{convection}} \tag{18}$$

where c_i and k_i represent the concentration and the diffusion coefficient of the vanadium ions in (mol/m^3) and (m^2/s), respectively, where i is the valence ($i = 2, 3, 4$, and 5). Furthermore, I_{shunt} denotes the shunt current in (A), J represents the current density in (A/m^2), Q is the flow rate in (m^3/s), d is the membrane thickness in (m), and S represents the area in (m^2), respectively. Furthermore, N, z, and F are the cell number, the Faraday constant, and the number of electrons transferred during the reaction, respectively. Superscripts t and c represent tank and cell, respectively, and subscripts n, p, M, and E represent the negative side, the positive side, the membrane, and the electrode cross-section, respectively.

Electrolyte volume variation and convection determine the concentration variations of vanadium ions in the tank. The concentrations of the four types of vanadium ions in the tank can be described by:

$$V_n^{t}\frac{\mathrm{d}c_2^{t}}{\mathrm{d}t} = \underbrace{2Q_n\left(c_2^{c} - c_2^{t}\right)}_{\text{convection}} - \underbrace{c_2^{t}\frac{\mathrm{d}V_n^{t}}{\mathrm{d}t}}_{\text{volume variation}} \tag{19}$$

$$V_n^t \frac{dc_3^t}{dt} = \underbrace{2Q_n\left(c_3^c - c_3^t\right)}_{\text{convection}} - \underbrace{c_3^t \frac{dV_n^t}{dt}}_{\text{volume variation}} \tag{20}$$

$$V_p^t \frac{dc_4^t}{dt} = \underbrace{2Q_p\left(c_4^c - c_4^t\right)}_{\text{convection}} - \underbrace{c_4^t \frac{dV_p^t}{dt}}_{\text{volume variation}} \tag{21}$$

$$V_p^t \frac{dc_5^t}{dt} = \underbrace{2Q_p\left(c_5^c - c_5^t\right)}_{\text{convection}} - \underbrace{c_5^t \frac{dV_p^t}{dt}}_{\text{volume variation}} \tag{22}$$

where V_n^t and V_p^t are the electrolyte volumes in the negative and positive tanks in (m^3), respectively.

2.3. Proton concentration dynamic submodel

Conventional models typically neglect variations in proton concentration and do not explicitly model the process. In this study, proton transport is accurately characterized through a dedicated submodel. In addition, a linear distribution of ion concentrations along the flow direction inside the cell is incorporated, and the electrolyte convection term is accordingly modified to reflect these spatial effects.

In addition to vanadium ions, the concentration of protons also varies over time. During the charging process of the VRB, protons move from the positive side to the negative side to maintain the electric neutrality of the electrolyte. A reverse process occurs during discharging. As vanadium ions diffuse from one side to the other, an equivalent number of protons with positive charges must move in the opposite direction to balance the charges [41]. Meanwhile, protons may be depleted or formed during the electrochemical reactions. Shunt current and convection can also influence proton concentration.

Within a short duration Δt, the proton concentration variations in the cell and tank due to the electrolyte flow rate are expressed by:

Positive and negative sides of the cell:

$$\begin{cases} \Delta c_{p,\mathrm{H}^+}^c V_{\mathrm{hc}} = 2Q_p\left(c_{p,\mathrm{H}^+}^t - c_{p,\mathrm{H}^+}^c\right)\Delta t \\ \Delta c_{n,\mathrm{H}^+}^c V_{\mathrm{hc}} = 2Q_n\left(c_{n,\mathrm{H}^+}^t - c_{n,\mathrm{H}^+}^c\right)\Delta t \end{cases} \tag{23}$$

Positive and negative sides of the tank:

$$\begin{cases} \Delta c_{p,\mathrm{H}^+}^t V_p^t = 2Q_p\left(c_{p,\mathrm{H}^+}^c - c_{p,\mathrm{H}^+}^t\right)\Delta t \\ \Delta c_{n,\mathrm{H}^+}^t V_n^t = 2Q_n\left(c_{n,\mathrm{H}^+}^c - c_{n,\mathrm{H}^+}^t\right)\Delta t \end{cases} \tag{24}$$

where c_{n,H^+}^c and c_{p,H^+}^c represent the proton concentrations of the negative side and positive side in the cell in (mol/m^3), respectively. c_{n,H^+}^t and c_{p,H^+}^t refer to the concentrations of protons in the tanks of the negative side and positive side in (mol/m^3), respectively.

By combining the mass balance and charge conservation laws, the dynamic equations of proton concentration are obtained as follows:

Negative side of the cell:

$$\begin{aligned} V_{\mathrm{hc}} \frac{\mathrm{d}c_{n,\mathrm{H}^+}^c}{\mathrm{d}t} = & \underbrace{\frac{2k_2c_2^cS_M}{d} + \frac{3k_3c_3^cS_M}{d} - \frac{4k_4c_4^cS_M}{d} - \frac{5k_5c_5^cS_M}{d}}_{\text{side reactions,charge conservation}} \\ & + \underbrace{\frac{NJS_E}{zF}}_{\text{main reactions}} - \underbrace{\frac{I_{\text{shunt}}}{zF}}_{\text{shunt current}} + \underbrace{2Q_n\left(c_{n,\mathrm{H}^+}^t - c_{n,\mathrm{H}^+}^c\right)}_{\text{convection}} \end{aligned} \tag{25}$$

Positive side of the cell:

$$\begin{aligned} V_{\mathrm{hc}} \frac{\mathrm{d}c_{p,\mathrm{H}^+}^c}{\mathrm{d}t} = & \underbrace{-\frac{4k_2c_2^cS_M}{d} - \frac{3k_3c_3^cS_M}{d} + \frac{2k_4c_4^cS_M}{d} + \frac{k_5c_5^cS_M}{d}}_{\text{side reactions,charge conservation}} \\ & + \underbrace{\frac{NJS_E}{zF}}_{\text{main reactions}} - \underbrace{\frac{I_{\text{shunt}}}{zF}}_{\text{shunt current}} + \underbrace{2Q_p\left(c_{p,\mathrm{H}^+}^t - c_{p,\mathrm{H}^+}^c\right)}_{\text{convection}} \end{aligned} \tag{26}$$

In the cell, the proton concentration is influenced by convection and the variation of electrolyte volume.

Tank on the negative side:

$$V_n^t \frac{dc_{n,\mathrm{H}^+}^t}{dt} = \underbrace{2Q_n\left(c_{n,\mathrm{H}^+}^c - c_{n,\mathrm{H}^+}^t\right)}_{\text{convection}} - \underbrace{c_{n,\mathrm{H}^+}^t \frac{dV_n^t}{dt}}_{\text{volume variation}} \tag{27}$$

Tank on the positive *side*:

$$V_p^t \frac{dc_{p,\mathrm{H}^+}^t}{dt} = \underbrace{2Q_p\left(c_{p,\mathrm{H}^+}^c - c_{p,\mathrm{H}^+}^t\right)}_{\text{convection}} - \underbrace{c_{p,\mathrm{H}^+}^t \frac{dV_p^t}{dt}}_{\text{volume variation}} \tag{28}$$

In the present model, species crossover through the membrane includes diffusion and convection contributions. The migration term is neglected due to the high supporting electrolyte concentration and the relatively weak electric potential gradient across the membrane under the investigated operating conditions [8,13,15].

2.4. Electrolyte volume dynamic submodel

Vanadium ions exist in the electrolyte in the form of hydration ions [12]. Thus, they carry a certain amount of water molecules across the membrane for crossover through the diffusion, affecting the volume of positive and negative electrolytes. Specifically, 1 mol of V^{2+} or V^{3+} will carry 6 mol of water molecules across the PEM, and 1 mol of VO^{2+} and 1 mol of VO_2^+ will carry 5 mol and 4 mol of water molecules across the membrane, respectively. According to Assumption 3, the density of the electrolyte remains constant. Hence, the volume change of the negative electrolyte $\Delta V_n^{\text{crossover}}$ can be obtained from

$$\Delta V_n^{\text{crossover}} = \sum_{i=2}^{5} \frac{M_i k_i c_i^c S_M \Delta t}{d\rho} \tag{29}$$

where M_i is the coefficient of electrolyte mass change in (kg/mol) caused by vanadium ions with valence state i crossing PEMs, and ρ denotes the initial electrolyte density in (kg/m^3).

Similar to vanadium ions, to balance the charge, the protons will transfer through the PEM during charging and discharging under the effect of the electro-osmotic force. Since the crossover of the protons carries water molecules ($H^+ \cdot 2.5H_2O$), the electrolyte volume will vary accordingly. The variation in the negative electrolyte volume $\Delta V_n^{\mathrm{C/D}}$ due to proton migration in time Δt is:

$$\Delta V_n^{C/D} = \frac{M_{\mathrm{hp}} J S_E \Delta t}{zF\rho} \tag{30}$$

where M_{hp} is the molar mass of hydrated protons in (kg/mol).

Homoplastically, the influence of shunt current on the negative electrolyte volume is:

$$\Delta V_n^{\text{shunt}} = -\frac{M_{\mathrm{hp}} I_{\text{shunt}} \Delta t}{zF\rho} \tag{31}$$

Proton transfer and vanadium ions crossover induce concentration gradients across the membrane, which in turn drive water migration via osmotic pressure [42]. The variation of negative electrolyte volume due to the osmotic pressure difference in Δt is described by

$$\Delta V_n^{\textit{pressure}} = \left|\vec{v}_{H_2O}^{\,m}\right| S_M \Delta t \frac{\rho_{H_2O}}{\rho} \tag{32}$$

where $\vec{v}^{m}_{H_2O}$ is the velocity of water across the membrane in (m/s) and ρ_{H_2O} denotes the water density in (kg/m^3).

According to the Van't Hoff equation, the difference in concentrations of vanadium ions and protons between the positive and negative electrolytes will produce osmotic pressure. As a result, water will cross the membrane in the opposite direction to the osmotic pressure drop. $\vec{v}^{m}_{H_2O}$ can be given by the alternate form of Schlogl's equation, which describes the convective transport of bulk electrolyte, i.e.,

$$\vec{v}^{m}_{H_2O} = -\frac{\kappa_p}{\mu_{H_2O}}\Delta p \tag{33}$$

where κ_p is the hydraulic permeability in (m^2), μ_{H_2O} is the viscosity of water in (Pa·s), and Δp represents the pressure drop.

Conventional methods do not consider the reduction in hydraulic pressure caused by volume imbalance between the positive and negative electrolytes. In this work, variation in hydraulic pressure is comprehensively characterized to enhance the accuracy of the hydraulic and electrochemical coupling analysis. Therefore, the modified Δp is calculated by

$$\Delta p = \frac{p_{osmotic} - p_{hydraulic}}{d} \tag{34}$$

where $p_{osmotic}$ and $p_{hydraulic}$ denote the osmotic and hydraulic pressure, respectively. Based on the Van 't Hoff equation, they are expressed by

$$p_{osmotic} = \left[\left(c_2^c + c_3^c + c_{n,H^+}^c\right) - \left(c_4^c + c_5^c + c_{p,H^+}^c\right)\right]RT \tag{35}$$

$$p_{hydraulic} = \rho g \frac{V_p^t - V_n^t}{S_t} \tag{36}$$

where R is the gas constant in (8.314 J/(mol·K)), T is the temperature in (K), and S_t represents the cross-sectional area of the tank in (m^2).

According to (33)–(36), (32) can be calculated as:

$$\Delta V_n^{pressure} = \frac{\kappa_p S_M \rho_{H_2O}\Delta t}{d\mu_\omega \rho} \times \left\{\left[\left(c_2^c + c_3^c + c_{n,H^+}^c\right) - \left(c_4^c + c_5^c + c_{p,H^+}^c\right)\right]RT - \rho g\frac{V_p^t - V_n^t}{S_t}\right\} \tag{37}$$

In summary, combining (29)–(31) and (37), the total volume change in the negative electrolyte in Δt can be calculated as

$$\Delta V_n^t = \Delta V_n^{crossover} + \Delta V_n^{C/D} + \Delta V_n^{shunt} + \Delta V_n^{pressure} \tag{38}$$

The final equations for the change of electrolyte volume are as follows:

Negative electrolyte:

$$\frac{dV_n^t}{dt} = \sum_{i=2}^{5}\frac{M_i k_i c_i^c S_M}{d\rho} + \frac{M_{hp} J S_E}{zF\rho} - \frac{M_{hp} I_{shunt}}{zF\rho} + \frac{\kappa_p S_M \rho_{H_2O}}{d\mu_{H_2O}\rho}\left\{\left[\left(c_2^c + c_3^c + c_{n,H^+}^c\right) - \left(c_4^c + c_5^c + c_{p,H^+}^c\right)\right]RT - \rho g\frac{V_p^t - V_n^t}{S_t}\right\} \tag{39}$$

Positive electrolyte:

$$\frac{dV_p^t}{dt} = -\frac{dV_n^t}{dt} \tag{40}$$

2.5. Electrochemical model

The electrochemical model describes its chemical behavior via multiple physical parameters. In a single cell, the cell voltage based on the ECM can be expressed as:

$$E_{cell} = E_{OCV} + \eta_{ohm} + \eta_{act} + \eta_{con} \tag{41}$$

where η_{act} is the activation overpotential, assuming that η_{act} can be neglected, as porous electrodes with a large effective surface area are used in a VRB. E_{OCV} is the open circuit voltage of a VRB, η_{ohm} is the ohmic overpotential, and η_{con} is the concentration overpotential. They are calculated by [39].

$$E_{ocv} = E_0 + \frac{RT}{zF}\ln\left(\frac{c_4^c c_5^c c_{H^+}^2}{c_2^c c_3^c}\right) \tag{42}$$

$$\eta_{ohm} = IR_{ohm} = JS_M R_{ohm} \tag{43}$$

$$\eta_{con} = \eta_{con}^{+} + \eta_{con}^{-} = \frac{RT}{zF}\ln\left(1 - \frac{J}{zFk_m c_r^+}\right) + \frac{RT}{zF}\ln\left(1 - \frac{J}{zFk_m c_r^-}\right) \tag{44}$$

where E_0 is the formal potential in (1.4 V) and R_{ohm} is the ohmic resistance in (Ω). In (44), η_{con}^{+} and η_{con}^{-} denote the concentration overpotential of positive and negative, respectively, c_r^+ and c_r^+ are the mole concentrations of positive and negative reactants in (mol/m^3), respectively, and k_m is the local mass transfer coefficient in (m/s). They are expressed by [15].

$$k_m = 1.6\times 10^{-3}\left(\frac{Q}{S_E}\right)^{0.4} \tag{45}$$

$$c_r^+ = \begin{cases} c_4^c, & \textbf{\textit{charging}} \\ c_5^c, & \text{discharging} \end{cases};\quad c_r^- = \begin{cases} c_3^c, & \textbf{\textit{charging}} \\ c_2^c, & \text{discharging} \end{cases} \tag{46}$$

Incorporating (42)–(44) into (41), for charging and discharging, the single-cell voltage can be calculated by

$$E_{cell} = E_0 + \frac{RT}{zF}\ln\left(\frac{c_4^c c_5^c c_{H^+}^2}{c_2^c c_3^c}\right) \pm JS_M R_{ohm} \pm \left|\frac{RT}{zF}\ln\left(1 - \frac{J}{zFk_m c_r^+}\right)\right| \pm \left|\frac{RT}{zF}\ln\left(1 - \frac{J}{zFk_m c_r^-}\right)\right| \tag{47}$$

For a stack consisting of N individual cells, the stack voltage is the sum of each cell voltage, i.e., $E_{stack} = NE_{cell}$. In this study, $N = 1$, corresponding to a single-cell configuration. The SOH and SOC are expressed by:

$$SOH = \frac{Q_{c,discharge}}{Q_{c,0}} \tag{48}$$

$$SOC = \min\left(\frac{c_2^t}{c_2^t + c_3^t}, \frac{c_5^t}{c_4^t + c_5^t}\right) \tag{49}$$

where $Q_{c,0}$ is the initial discharge capacity of VRB.

In summary, the coupling relationship among the above models is illustrated in Fig. 3.

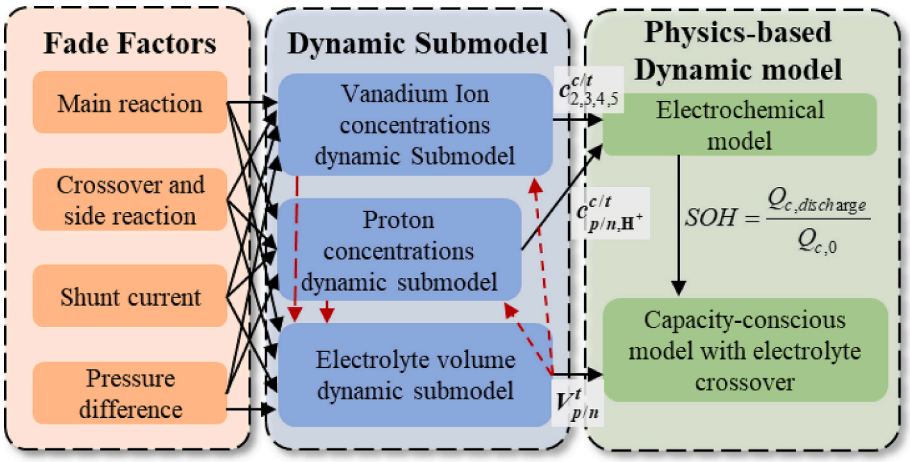


Fig. 3. Coupling relationship among degradation factors, dynamic submodels, and the dynamic model with electrolyte crossover.

Table 2
VRB model parameters.

Symbol	Meaning	Value	Remark
N	Number of cells	1	Preset
V_c	Volume of the half-cell	12.9 mL	Preset
V_p^t	Volume of the positive tank	30 mL	Preset
V_n^t	Volume of the negative tank	30 mL	Preset
T	Temperature	298.2 K	Preset
I_{shunt}	Shunt current	0	Measured
R	Universal gas constant	8.314 J/(mol·K)	Calculated
Q_p	Positive flow rate	30 ml/min	Preset
Q_n	Negative flow rate	30 ml/min	Preset
d	Membrane thickness	1.25×10^{-4} m	Preset
z	number of electrons transferred during the reaction	1	[13]
κ_p	Hydraulic permeability	1.58×10^{-18} m^2	[13]
J	Current density	80 mA/cm^2	Preset
S_M	Effective membrane area	25×10^{-4} m^2	Measured
S_E	Electrode cross-sectional area	2.175×10^{-4} m^2	Measured
ρ_{H_2O}	Water density	1×10^3 kg/m^3	Calculated
ρ	Initial Electrolyte density	1.354×10^3 kg/m^3	[8]
F	Faraday's constant	96,485C/mol	[13]
μ_{H_2O}	Viscosity of water	8.684×10^{-4} Pa·s	Calculated
κ_p	Hydraulic permeability	1.58×10^{-18} m^2	[13]
M_2	Molar mass of V^{2+} particles with bound water	−0.159 kg/mol	Calculated
M_3	Molar mass of V^{3+} particles with bound water	−0.159 kg/mol	Calculated
M_4	Molar mass of VO^{2+} particles with bound water	0.157 kg/mol	Calculated
M_5	Molar mass of VO_2^+ particles with bound water	0.155 kg/mol	Calculated
M_{hp}	Molar mass of hydrated protons	4.6×10^{-2} kg/mol	[8,13]
k_2	Diffusion coefficient of V^{2+}	8.8×10^{-12} m^2/s	[7,8]
k_3	Diffusion coefficient of V^{3+}	3.2×10^{-12} m^2/s	[7,8]
k_4	Diffusion coefficient of VO^{2+}	6.8×10^{-12} m^2/s	[7,8]
k_5	Diffusion coefficient of VO_2^+	5.9×10^{-12} m^2/s	[7,8]
g	Gravitational acceleration	9.8 m/s^2	Calculated
S_t	Cross-sectional area of the tank	7.07×10^{-4} m^2	Calculated

3. Experimental setups

3.1. Simulation environment

The proposed model is implemented in MATLAB 2023a on a computer with an Intel(R) Core(TM) i7–10700KF CPU @3.80 GHz, NVIDIA GeForce RTX 3070 (8GB) of GPU, and 16 GB of memory, with the model parameters specified in Table 2. The simulation sampling frequency is set to 1 Hz, corresponding to a time step of 1 s. The total simulation time corresponded to more than 1,200,000 s of operation over 300 cycles. The simulation model is configured using the same operating conditions as the experimental setup.

3.2. Experimental environment

To validate the proposed model, a lab-scale VRB experimental platform is constructed, as shown in Fig. 4. The platform consists of three main components: a battery test system, a host computer, and a single-cell VRB system. The battery test system (Neware BTS 7.6×) converts the received control instructions into electrical signals and transmits them to the battery, while collecting voltage and current data. They are connected through a local area network. The host computer provides control instructions and visualizes the collected data. The VRB system (Wuhan Zhisheng New Energy Co., Ltd.) consists of a single-cell VRB stack (Nafion 212 membrane, carbon felt electrodes measuring 5 cm × 5 cm × 0.435 cm), two electrolyte tanks, and two peristaltic pumps (DIP-KPK400, Kamoer). The positive and negative electrolytes were stored in covered electrolyte tanks during cycling, with the circulation tubes connected to the tanks through the tank covers. The tanks were kept closed throughout the charge–discharge tests to minimize direct exposure of the vanadium electrolytes to ambient air and thereby reduce possible oxidation of V(II) by dissolved oxygen. The detailed specifications of the experimental platform are summarized in Table 2. Electrolyte viscosity is not explicitly listed as it is not directly involved in the governing equations, but is implicitly reflected in transport-related parameters. Furthermore, the operating conditions used in the simulation, including current density and flow rate, are identical to those in the experimental tests, ensuring a direct and consistent comparison.

Although the tank volume is not scaled with cell size, this primarily affects the time scale of capacity fade rather than the underlying mechanisms, which are governed by species transport and remain unchanged [10].

For the single-cell system studied here, the I_{shunt} is set to zero in the validation cases. The shunt-current term is retained only in the general formulation to preserve model completeness and facilitate extension to practical multi-cell systems.

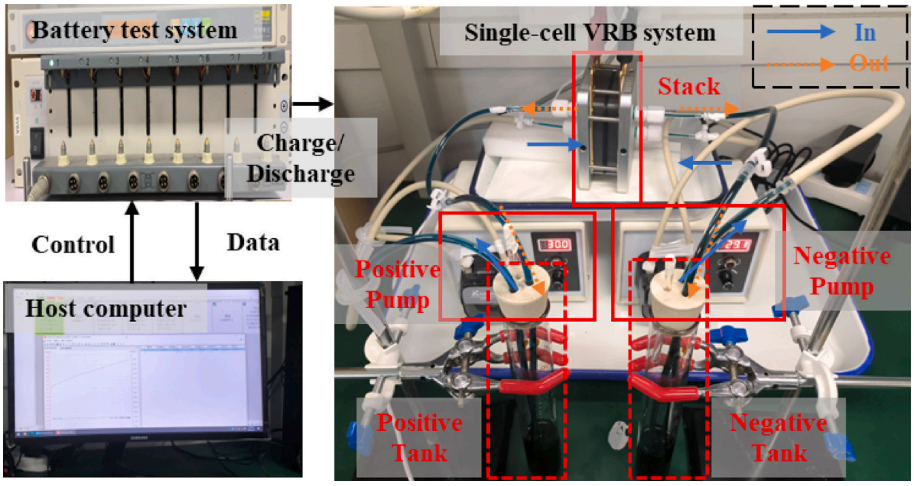


Fig. 4. Experimental platform for VRB performance evaluation.

The experiments are conducted under laboratory ambient conditions with a stable room temperature (25 °C). Although an active thermal management system was not employed in the present test bench, the environmental temperature variation during cycling was limited, thereby reducing the influence of external temperature fluctuations on battery performance. In addition, the operating current densities investigated in this work were moderate, and no obvious abnormal temperature rise was observed during long-term cycling. Both positive and negative tanks have identical dimensions (radius: 30 mm; height: 215 mm), yielding an approximate volume of 100 mL. The initial electrolyte volume is around 30 mL per tank. The total vanadium ion concentration is 1.7 mol/L. Electrolyte is an average valence state of 3.5. Electrolyte compositions contain 1.7 M vanadium and 4.7 M H_2SO_4. Before the charging/discharging cycle test, several prior cycles are performed to fully mix the cathode and anode electrolytes and activate the system. During this process, $V^{3.5+}$ is completely converted to V^{2+}/V^{3+} in the negative electrolyte, and VO^{2+}/VO_2^+ in the positive electrolyte. Electrolyte circulation between the cell and tanks is driven by peristaltic pumps. Although the experimental platform supports a wide range of flow rates (0.1–240 mL/min), a fixed flow rate of 30 mL/min is used in this study for both experiments and simulations. The selected flow rate is consistent with previously reported studies [13,15–17], and is intentionally chosen to enhance transport limitations for more stringent model validation. The cycle protocol requires the battery to be charged to 1.7 V at a constant current density of 80 mA/cm2 (2 A), followed by discharge to 1.1 V at the same current density. SOC corresponds to 10–90%. This charge-discharge process is repeated for a total of 300 cycles.

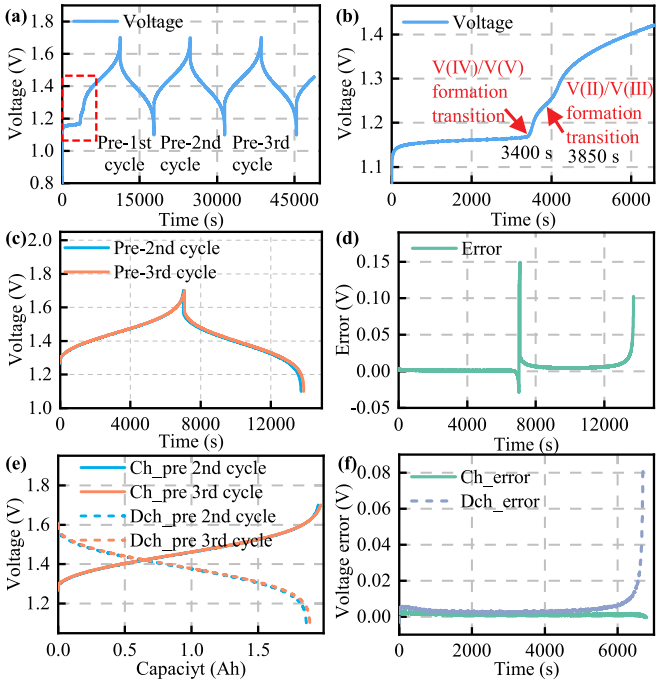


Fig. 5. Formation charge process. (a) Initial cycling. (b) First cycle (zoomed-in view). (c) Voltage profiles in the 2nd and 3rd cycles; (d) Voltage error between the 2nd and 3rd cycles. (e) Capacity-voltage profiles of the charging and discharging process in the 2nd and 3rd cycles. (f) Voltage error of the charging and discharging process between the 2nd and 3rd cycles.

3.3. Preliminary experiment design

Due to the properties of Nation membrane, the electrolyte volumes in the positive and negative tanks change rapidly during the very first cycles [9]. Therefore, during this preliminary activation process, vanadium ion crossover and water migration inevitably induce electrolyte concentration imbalance and volume imbalance. These accumulated deviations directly affect the observed degradation behavior in subsequent aging experiment, thereby reducing the repeatability and comparability of the experimental results. A two-step preliminary experiment is designed to eliminate initial electrolyte imbalance and improve long-term aging observation reliability. This procedure ensures that the observed electrolyte volume transfer and capacity decay originate from electrochemical processes (e.g., electro-osmosis, osmosis, and side reactions), rather than from initial state imbalance. Specifically,

Step 1*: *Initial Formation. Commercial electrolyte with an average valence of 3.5 is circulated within the system to achieve thorough mixing and to complete the initial valence separation and formation. It consists of two steps:

Step 1.1: *Initial Filling*. Equal volumes (30 mL each) of the commercial 3.5-valent electrolyte are filled into the positive and negative tanks, respectively.

Step 1.2: *Formation charge*. The VRB is cycled for three cycles at a low current density of 40 mA/cm^2 until the time-voltage and capacity-voltage profiles become stable and reproducible. During this stage, electrolyte volume transfer is allowed and expected to occur. This step serves to activate the system rather than to evaluate battery performance.

In the present work, the commercially fresh electrolyte initially consisted of the equal volume of V^{3+} and VO^{2+} (1.7 M $V^{3.5+}$ + 4.7 M

H_2SO_4). Hence, before the formal long-term aging experiment, a formation charge process is necessary to convert the mixed electrolyte into negative electrolyte containing V^{2+}/ V^{3+} and positive electrolyte containing VO^{2+}/VO_2^+, thereby establishing the normal initial operating state of the VRB system [43], as shown in Fig. 5(a). During the formation charge, the two redox couples, V(II)/V(III) and V(IV)/V(V), evolve concurrently because the initially mixed electrolyte is present on both sides of the cell. The transient features (about 3400 s and 3850 s) highlighted in Fig. 5b therefore represent the progressive valence-separation process rather than the onset of two independent redox reactions.

Figs. 5(c) and (e) illustrate that the time-voltage and capacity-voltage profiles become progressively more stable after the first cycle. The small voltage and capacity differences between the 2nd and 3rd cycles, as shown in Fig. 5(d) and (f). The electrochemical response thus reaches a relatively stable and reproducible state, signifying completion of the formation charge process. Therefore, three preliminary cycles are employed to activate the VRB system before the long-term aging experiment.

***Step 2*: System Reset and Standardization**. This step resets the system to a well-defined, balanced initial state before the aging tests. It consists of three steps:

Step 2.1: *Stop at 50% SOC*. Following *Step 1.2*, the battery is charged to 50% SOC. At this operating point, ion concentrations, electrolyte densities, and osmotic pressures on the positive and negative sides are most similar, thereby minimizing the driving force for water migration due to concentration differences. This represents the optimal timing for electrolyte adjustment and volume rebalancing.

Step 2.2: *Electrolyte Mixing and Rebalancing*. All electrolyte from both sides is completely removed and thoroughly mixed in a clean, dry container. This process re-homogenizes the valence distribution, returning it to a near average state that is equivalent to a brand-new but already activated electrolyte. Any composition differences by side reactions or uneven migration during the initial formation stage are eliminated. After remixing, spontaneous redox equilibration occurs among vanadium species (e.g., $V^{2+} + VO_2^+ \rightarrow V^{3+} + VO^{2+}$), leading to a thermodynamically balanced electrolyte with an average valence state close to $V^{3.5+}$. This state is widely regarded as the standard fully mixed condition in VRB systems and provides a consistent baseline for subsequent experiments.

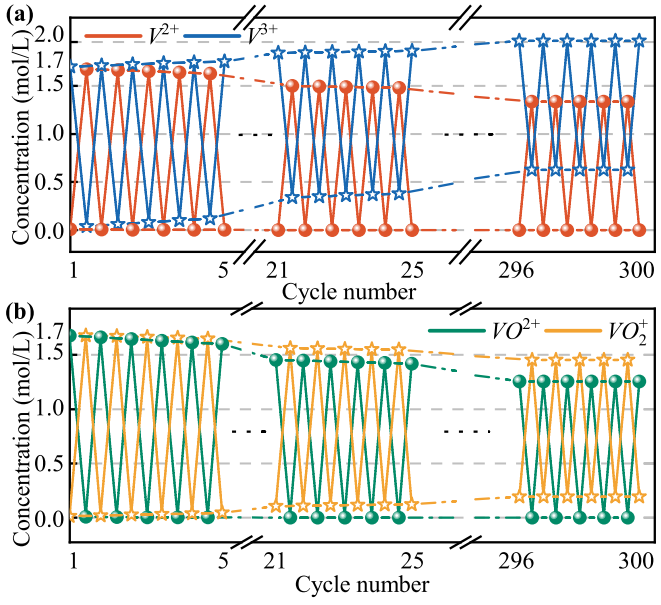


Fig. 6. Variations of vanadium ion concentrations in the tank. (a) Negative side (V^{2+} and V^{3+}); (b) Positive side (VO^{2+} and VO_2^+).

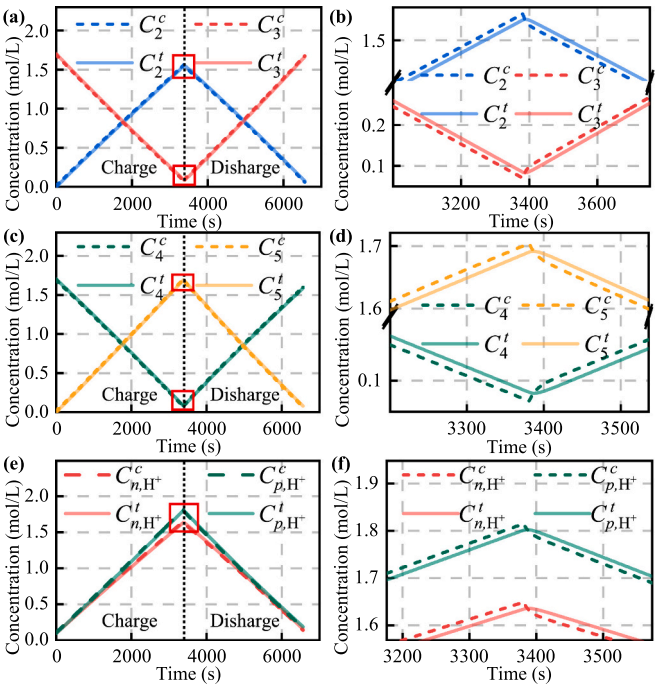


Fig. 7. Comparison of simulated species concentrations in the cell and tanks for (a) V^{2+} and V^{3+}; (b) V^{2+} and V^{3+} (zoomed-in view); (c) VO^{2+} and VO_2^+; (d) VO^{2+} and VO_2^+ (zoomed-in view); (e) H^+ in the positive and negative sides [44]; (f) H^+ in the positive and negative sides (zoomed-in view).

Step 2.3: *Re-fill With Equal Volumes*. The thoroughly mixed electrolyte is evenly divided and refilled into the positive and negative tanks with equal volume, restoring the system to a balanced and reproducible initial condition for subsequent aging experiments.

4. Illustrative examples

4.1. Simulation results and discussion

During the 300-cycle charge/discharge test, the variation of vanadium ion concentrations across the four valence states at the positive and negative tanks is illustrated in Fig. 6. Vanadium ion concentrations increase at an accelerating rate with the number of charge-discharge cycles. According to the Nernst equation, OCV is directly influenced by the concentrations of the vanadium ions. During long-term operation, the increasingly uneven concentration distribution causes the terminal voltage to reach the cut-off threshold earlier, leading to shorter charging and discharging durations.

Since the cell and tank are connected by pipes, the electrolyte circulates through pipes between the cell and tank. It follows that there is a difference in the distribution of reactant concentrations between the cell and tanks. Fig. 7 shows the model-predicted results in vanadium ion and proton concentration distribution between the cell and tank. The reactant concentration in the tank always lags behind that of the cell. This is because the redox reactions take place in the cell first, and the concentration in the tank is affected by the flow rate later. When it comes to the charge-discharge turning point, in a cell, there is a short period of plunge or surge in reactant concentration, which is caused by a combination of the main reactions and convection. Fig. 7 highlights the necessity of distinguishing between cell and tank dynamics, as the commonly used well-mixed assumption may lead to inaccuracies in capturing transient behavior and long-term degradation.

Fig. 8 illustrates the influence of four factors on the electrolyte volume during the first and the last cycles. Both II (main reaction) and IV (osmotic pressure difference) have a significant impact on volume

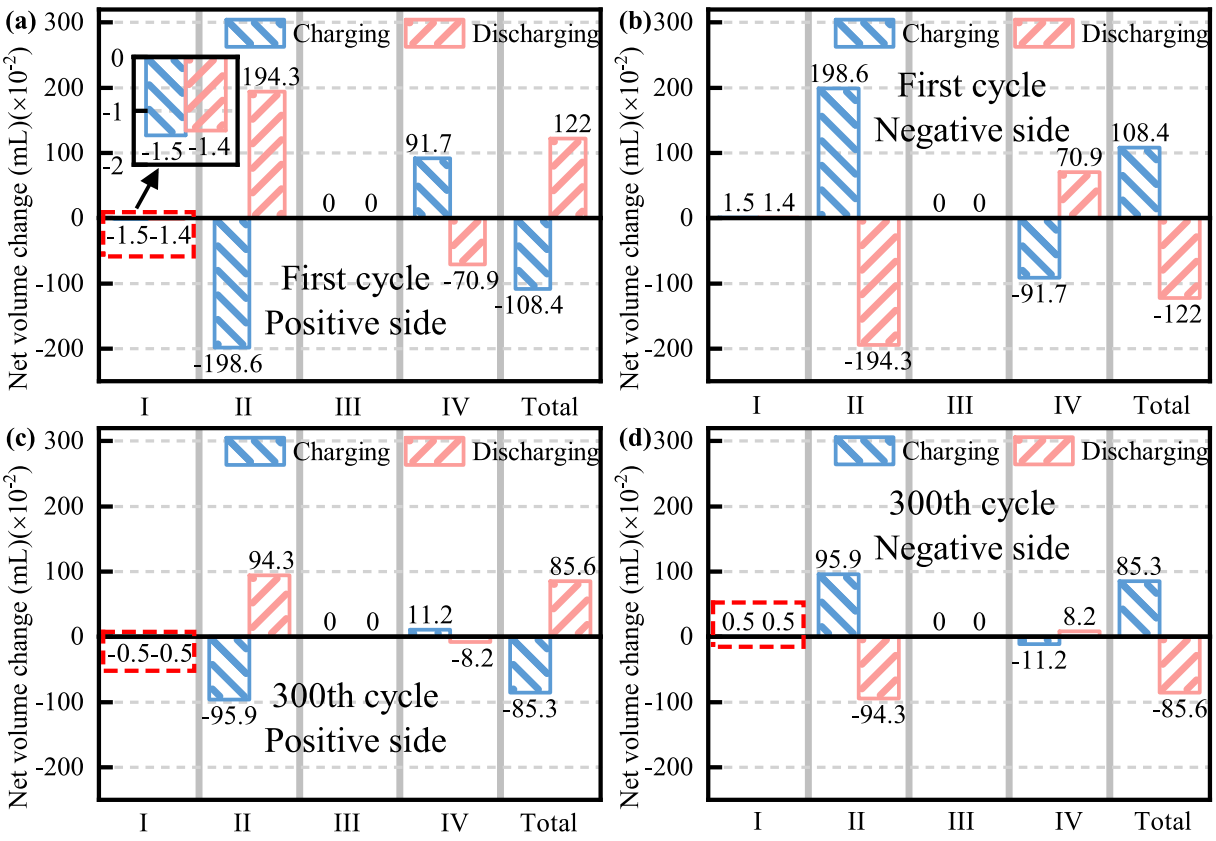


Fig. 8. Contributions of different transport mechanisms to the net electrolyte volume change during representative cycles. (I: Diffusion, II: Electro-osmotic, III: Shunt current, IV: Osmotic) during representative cycles. (a) First cycle on the positive side. (b) First cycle on the negative side. (c) 300th cycle on the positive side. (d) 300th cycle on the negative side.

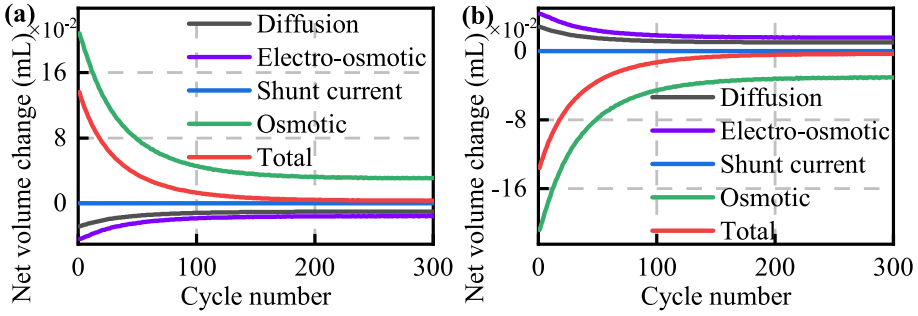


Fig. 9. Cycle-dependent evolution of electrolyte volume variation associated with different transport mechanisms for (a) Positive side. (b) Negative side.

Table 3
Contribution analysis of different transport mechanisms to electrolyte volume imbalance.

Mechanism	Driving force	Net water transfer
Diffusion (I)	Concentration gradient	Less significant
Electro-osmotic drag (II)	Proton transport	Theoretically neglected
Osmotic transport (IV)	Osmotic pressure difference	Primary

variation. Specifically, water migration driven by the osmotic pressure difference is identified as the primary cause of electrolyte volume imbalance. Although the main reaction substantially affects the volume during charging and discharging, its contribution to the net volume transfer is so small that it can be theoretically neglected, which is consistent with previous research findings [12,13]. It should be noted that Fig. 8 presents the net volume variation of the electrolyte during the representative cycles rather than the cumulative water crossover throughout the aging process.

To further examine the long-term evolution of these transport-induced volume variations, the corresponding electrolyte volume variations are plotted as a function of cycle number in Fig. 9. The volume variations associated with the different transport mechanisms evolve progressively with cycle number and gradually approach relatively stable values. The pronounced changes during the initial cycles are mainly associated with the transient adjustment of the electrolyte transport state, including the establishment of concentration gradients and dynamic crossover equilibrium. With continued cycling, the driving forces for some transport processes gradually evolve toward a quasi-steady state, resulting in a reduced incremental volume variation per cycle. However, the cumulative water crossover and the resulting electrolyte imbalance continue to accumulate throughout cycling, although the accumulation rate progressively decreases.

Table 3 illustrates the contribution analysis of three main transport mechanisms (I, II, and IV) to electrolyte volume. Specifically,

1) **Diffusion**. It is driven by concentration or potential gradients, corresponding to "I". Since commercial membranes typically achieve a high coulombic efficiency exceeding 95%, the contribution of diffusion on net water migration is considered insignificant.
2) **Electro-osmotic drag**. It is driven by proton coupled water transport during the main reaction to balance chargers, corresponding to "II". Song et al. [10] have experimentally demonstrated that this term causes certain electrolyte volume changes during charging and discharging. However, these volume changes do not theoretically accumulate over consecutive charge discharge cycles.
3) **Osmotic transport**. As vanadium ion crossover continuously accumulates during cycling, the concentration imbalance gradually increases, resulting in the osmotic pressure difference across the membrane based on (35). This osmotic pressure difference continuously drives water molecules to migrate toward the electrolyte with higher ion concentration, thereby causing electrolyte volume imbalance during long-term operation. In addition, the hydrated structure and relatively high-water permeability of the Nafion membrane further enhance osmotic-driven water transport.

Several mitigation strategies may be considered to alleviate long-term capacity fading in VRB systems. Optimizing membrane properties, appropriate operating conditions, and periodic electrolyte remixing or electrolyte rebalancing strategies can mitigate concentration and volume imbalance accumulation during long-term cycling. The proposed model may provide useful guidance for evaluating the influence of these operating and material parameters on long-term degradation behavior and for optimizing VRB operational strategies.

4.2. Experimental results and discussion

To evaluate the long-term predictive capability of the proposed VRB aging model, a comprehensive validation was conducted over 300 continuous charge-discharge cycles under the operating conditions described in Section 3.2, namely, a flow rate of 30 mL/min, a current density of 80 mA/cm^2, and a voltage range of 1.1–1.7 V. A comparison between the simulated and experimental voltage profiles is conducted for the final cycle as a representative example, as shown in Figs. 10(b) and (c). A voltage error result of less than 0.03 V shows good agreement with the experimental voltage profiles during both charging and discharging processes. The model can accurately capture the voltage plateau evolution and polarization characteristics of the VRB system. Furthermore, Fig. 11 demonstrates high fidelity between the other simulated and experimental data. Specifically, the model accurately captures the non-linear degradation of SOH. After 300 cycles, the experimental SOH is 0.61149, the simulated SOH is 0.62059, resulting in an error of 0.0091. The relative SOH error remains within a narrow corridor of less than 5.33% throughout the stabilization phase, as shown in Fig. 11(b). Furthermore, the complex volume variations driven by ion and water crossover are successfully tracked with a max error of 5.58%, as shown in Fig. 11(d). The model prediction efficiency (e.g., CE, VE, and EE) exhibits high accuracy with deviations confined to within ±0.67%, as shown in Fig. 11(f). Table 4 illustrates close agreement across multiple physical domains, including voltage, SOH, electrolyte volume, and efficiency, demonstrating the model's efficacy in diagnosing degradation mechanisms and predicting the service life of VRB systems.

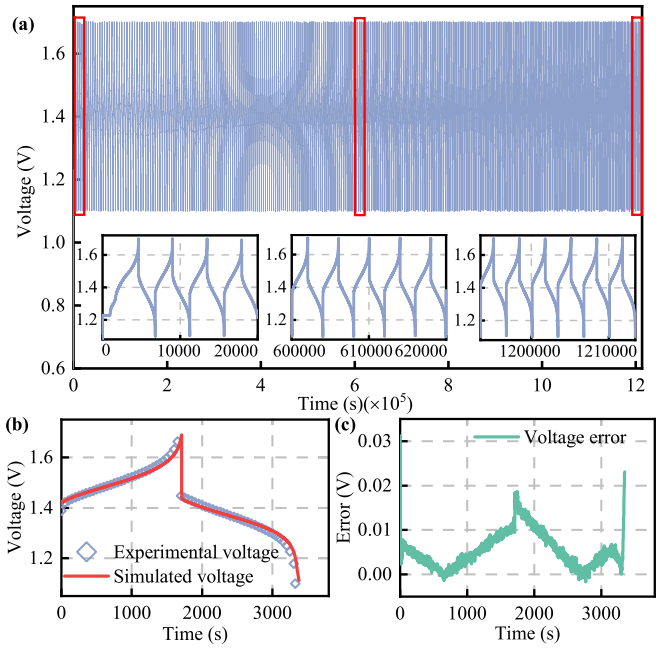


Fig. 10. Experimental and simulated voltage. (a) Experimental terminal voltage. (b) Voltage validation for the final cycle. (c) Voltage error for the final cycle.

In Figs. 11(a) and (c), the relatively larger deviations of SOH and volume observed during the initial cycles are mainly associated with transient non-equilibrium processes, including rapid membrane hydration, electrolyte redistribution, and the establishment of dynamic crossover equilibrium [9,42]. After the initial equilibration stage, the system behavior becomes more stable, resulting in improved agreement between simulation and experiment.

Fig. 12 shows the evolution of the electrolyte in the positive and negative tanks at the end of charge (EOC) and end of discharge (EOD) over the 300-cycle aging test. A progressive volume imbalance is observed, with electrolyte gradually accumulating in the positive tank and decreasing in the negative tank. This behavior provides direct experimental evidence of net water and vanadium species crossover through the ion-exchange membrane, primarily driven by osmotic pressure and electro-osmotic drag.

It should be noted that slight discrepancies can be observed between the positive and negative electrolyte volume variations in the experimental results during long-term cycling. In practice, the electrolyte transport and redistribution processes are influenced by multiple factors, including local electrolyte retention within porous electrodes and flow channels, circulation delay in the external piping system, and measurement uncertainty associated with electrolyte volume monitoring.

In addition, the present model adopts idealized assumptions, including spatially averaged transport behavior and homogeneous electrolyte mixing, which tend to produce more symmetric volume evolution between the positive and negative electrolytes. Nevertheless, the proposed model successfully captures the overall long-term evolution trend of electrolyte imbalance, indicating that the dominant transport mechanisms are reasonably represented.

4.3. Model comparison

The traditional model fails to consider the impact of electrolyte volume change on ion concentration, and a complete physics-dynamic model has yet to be established. The comparative performance of the proposed model and a traditional VRB model reported in [13,17] is illustrated in Fig. 13. The proposed model exhibits closer agreement with the reference line (red) and with the measured data over the entire degradation trajectory. In contrast, the traditional model demonstrates a pronounced nonlinear deviation as SOH declines, which can be attributed to its limited ability to capture the stoichiometric imbalance and crossover-induced capacity drift.

From a statistical perspective, the proposed model achieves

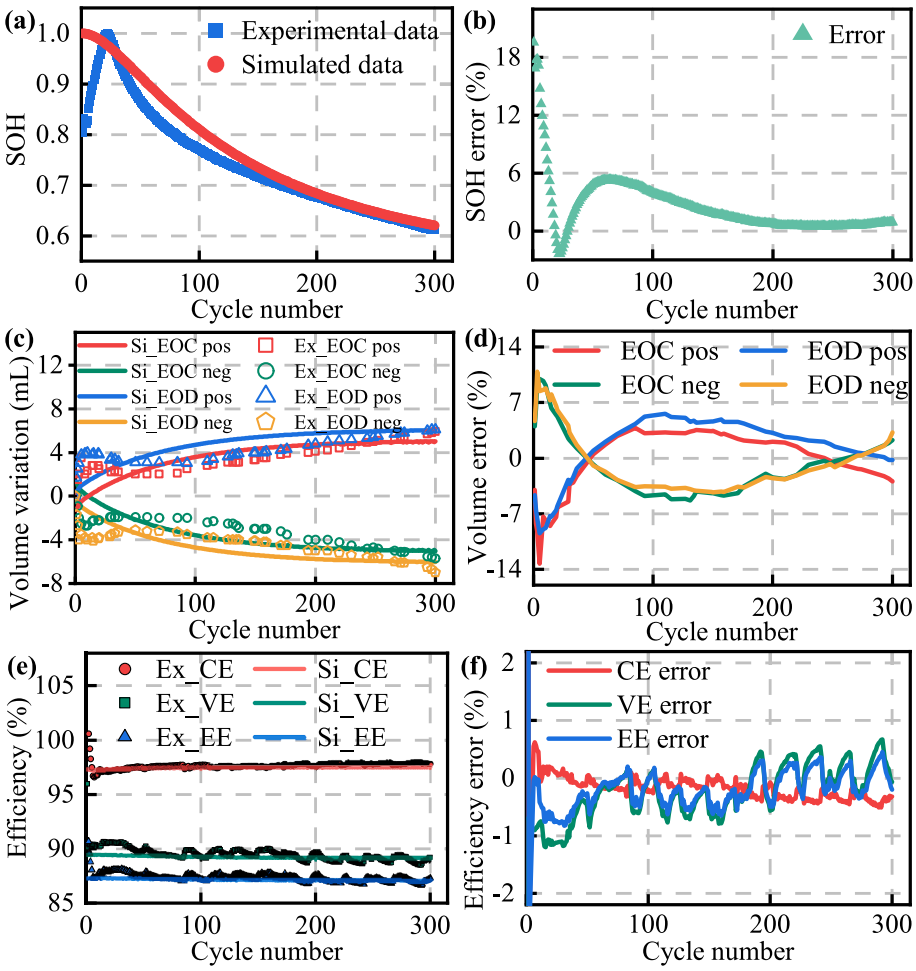


Fig. 11. Experimental and simulated results. (a) SOH validation. (b) SOH error. (c) Electrolyte volume variation validation. (d) Volume variation error. (e) CE, VE, and EE. (f) Efficiency error.

Table 4
Statistical error analysis of the proposed model for multivariable predictions.

Variables		RMSE	
Voltage		0.0069 V	
SOH	Entire	3.901%	
	Stabilization	2.673%	
Electrolyte volume	At EOC pos	1.3759 mL	Average: 1.3708 mL
	At EOC neg	1.3587 mL	
	At EOD pos	1.3905 mL	
	At EOC neg	1.3579 mL	
Efficiency	CE	2.938%	Average: 2.02%
	VE	0.633%	
	EE	2.488%	

improved accuracy compared with the traditional model. As summarized in Table 5, the average SOH error is reduced from 5.91% to 2.58%, corresponding to a 56.3% reduction in mean error magnitude. In addition, the error distribution shown in Fig. 13(b) indicates that the majority of error entries for the proposed model are concentrated within the [0, 0.06] range, with a pronounced peak near zero. By contrast, the error distribution of the traditional model spans a wider range of [0.02, 0.1], as shown in Fig. 13(d). These results demonstrate that the proposed model provides more consistent performance in representing the long-term degradation behavior of VRB systems.

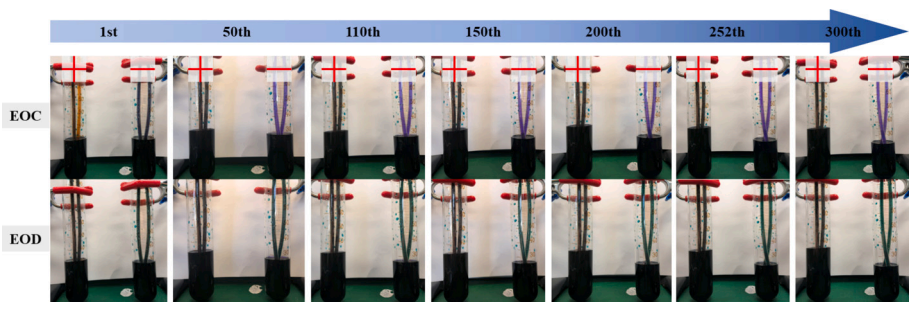


Fig. 12. Experimental result of electrolyte volume of VRB for 300 charge-discharge cycles.

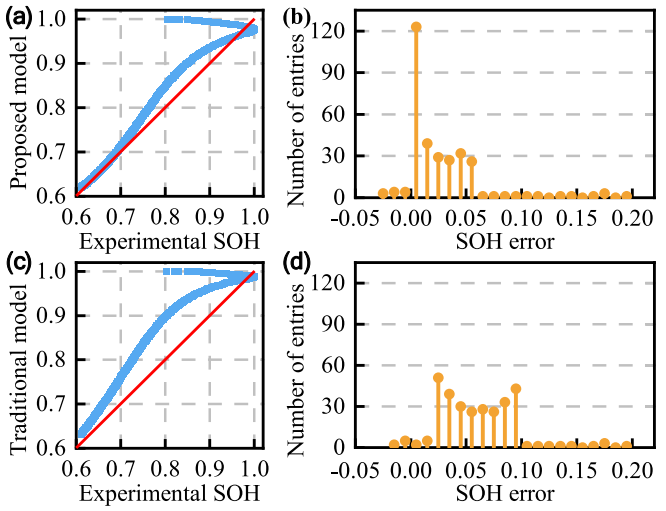


Fig. 13. SOH validation of different models. (a) Proposed model. (b) Error frequency distribution of the proposed model. (c) Traditional model. (d) Error frequency distribution of the traditional model.

Table 5
Model SOH error distribution.

Frequency	Traditional model	Proposed model
Majority range (≥90%)	[0.02, 0.1] 276/300 = 92%	[0, 0.06] 276/300 = 92%
Minority range (<10%)	[−0.02,-0.02)& (0.1,0.2] (14 + 10)/300 = 8%	[−0.03, 0)&(0.06, 0.2] (11 + 13)/300 = 8%
Average error	5.91%	**2.58%**

Table 6
Cell parameters and experimental results.

Items	Cell 1#	Cell 2#	Cell 3#
Electrode size (cm × cm)	5 × 5	5 × 5	3 × 3
Current density (mA/cm^2)	80	120	200
(+/−) Flow rate (mL/min)	30	30	50
Cycle number	300	300	200
(+/−) Cell volume (mL)	12.9	12.9	10
(+/−) Tank volume (mL)	30	30	20
(+) Volume difference (mL)	6.1	4.6	3.3
(+) Difference percentage	20.33%	15.33%	16.5%
(−) Volume difference (mL)	7	6.2	4
(−) Difference percentage	23.33%	20.67%	20%
Rated capacity (Ah)	1.7487	1.6656	1.1209
Final capacity (Ah)	1.0693	0.9353	0.8073
Capacity fade	38.85%	43.85%	27.98%

4.4. Analysis and validation under different current densities and cell sizes

To further evaluate the applicability of the proposed model under different investigated operating conditions, cross-validation is performed across the other two cell configurations (Cells 2–3#) under different operating conditions (see Table 6), in addition to the previously used Cell 1#. Cell 2#, operated at a higher current density of 120 mA/cm^2, exhibits more pronounced capacity fade (43.85%) compared with Cell 1# (38.85%). The flow rate is kept constant across different current densities to investigate the effect of current density on capacity fade under consistent operating conditions and to provide a comprehensive validation of the proposed model. For Cell 3#, which features a reduced electrode area (3 cm × 3 cm) and a higher current density of 200 mA/cm^2, the proposed model continues to provide accurate predictions, indicating its applicability across varying cell designs and operating ranges.

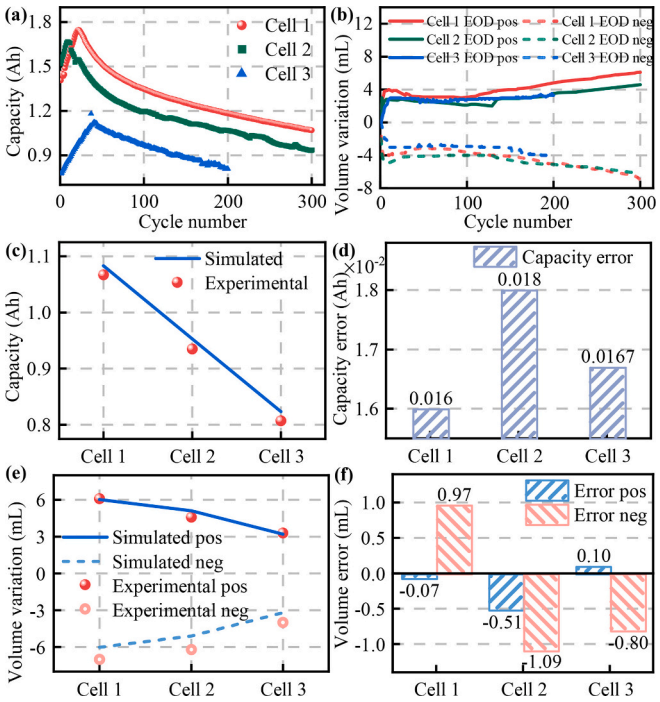


Fig. 14. Experimental and simulated results of Cells 1–3# for long-term operation. (a) Capacity decay. (b) Electrolyte volume variation at EOD. (c) Capacity validation. (d) Capacity error. (e) Volume variation validation. (f) Volume variation error.

As shown in Figs. 14(c) and (d), the absolute capacity errors for all three cells remain below 0.018 Ah, highlighting the model's fidelity in tracking degradation regardless of cell scale or load intensity. In addition, the electrolyte volume variations are compared with experimental results in Fig. 14(e). The corresponding volume errors on the positive and negative sides are generally within ±1.09 mL for all cells, as shown in Fig. 14(f). These results suggest that the proposed framework applies to long-term VRB performance prediction under varying system specifications and current densities.

The different capacity fading rates observed under various current densities are mainly associated with the coupled effects of crossover accumulation time and electrolyte imbalance evolution. At lower current densities, the charge–discharge duration of each cycle becomes longer, which increases the residence time for membrane transport processes and allows crossover-induced imbalance to accumulate more significantly during cycling. In contrast, higher current densities shorten the cycling duration and reduce the effective transport time available for ion crossover and water migration, thereby slowing the long-term imbalance accumulation to some extent.

The prediction deviations are mainly associated with the coupled effects of membrane transport behavior, electrochemical kinetics, and mass transfer limitations. Specifically,

1) **Different current densities**. At relatively low current densities, the longer cycling duration increases the cumulative impact of vanadium ion crossover and water migration, making the model predictions more sensitive to membrane flux assumptions and electrolyte redistribution behavior. In contrast, higher current densities shorten the cycling duration and reduce the effective transport time available for ion crossover and water migration, thereby slowing the long-term imbalance accumulation to some extent. At higher current densities, concentration polarization and local reaction non-uniformity become more significant, while the present transient lumped-parameter model assumes spatially averaged transport and

Table 7
VRB model preset parameters and their boundaries for parameter sensitivity analysis.

Symbol	Meaning	Value	Boundaries
k_2	Diffusion coefficient of V^{2+}	8.8×10^{-12} m^2/s	7.04×10^{-12}–10.56×10^{-12}
k_3	Diffusion coefficient of V^{3+}	3.2×10^{-12} m^2/s	2.56×10^{-12}–3.84×10^{-12}
k_4	Diffusion coefficient of VO^{2+}	6.8×10^{-12} m^2/s	5.2×10^{-12}–7.8×10^{-12}
k_5	Diffusion coefficient of VO_2^+	5.9×10^{-12} m^2/s	4.72×10^{-12}–7.08×10^{-12}
d	Membrane thickness	1.25×10^{-4} m	10^{-4}–1.5×10^{-4}
ρ	Initial electrolyte density	1.354×10^3 kg/m^3	1.0832×10^3–1.6248×10^3
κ_p	Hydraulic permeability	1.58×10^{-18} m^2	1.264×10^{-18}–1.896×10^{-18}

Table 8
Model predictions for parameters varied within a ± 20% range.

Parameter		κ_p	ρ	d	k_i
SOH	$SOH_{-20\%}$	0.6598	0.6563	0.6168	0.6604
	SOH_0	0.6206			
	$SOH_{+20\%}$	0.6191	0.6205	0.6566	0.6195
Volume difference (mL)	$VD_{-20\%}$	12.2517	12.155	11.9772	12.1688
	VD_0	12.0676			
	$VD_{+20\%}$	12.1022	12.0424	12.0948	12.049

reaction behavior. Consequently, local kinetic variations cannot be fully captured.

2) **Different flow rates**. Lower flow rates aggravate concentration gradients and mass transfer limitations within porous electrodes and flow channels, whereas higher flow rates improve electrolyte mixing uniformity and reduce local concentration polarization, thereby improving the applicability of the lumped-parameter assumption.
3) **Different cell sizes**. Larger battery sizes may introduce stronger spatial non-uniformity in electrolyte flow and local electrochemical activity, which are difficult to fully resolve using a zero-dimensional transient framework.

4.5. Sensitivity and uncertainty analysis of key parameters

To further evaluate the robustness of the proposed model and quantify the influence of parameter uncertainty on the prediction results, a one-at-a-time (OAT) sensitivity analysis is performed for several key model parameters, including the membrane hydraulic permeability (κ_p), membrane thickness (d), vanadium-ion diffusion coefficients (k_i), and initial electrolyte density (ρ). They are derived from the uncertainty analysis principle that is highly uncertain and has a physical impact on the results.

Considering the uncertainties associated with literature-reported values and parameter fitting procedures, each parameter is independently varied by ±20% around its baseline value while keeping all other parameters unchanged. Table 7 lists the VRB model preset parameters and their boundaries for parameter sensitivity analysis. Table 8 illustrates the effects on the predicted SOH and electrolyte volume imbalance after 300 cycles are evaluated.

To quantitatively compare the sensitivity of different parameters, a normalized sensitivity coefficient (SC) is defined using a central-difference approximation:

$$SC = \frac{Y_{+20\%} - Y_{-20\%}}{0.4 Y_0} \times 100\% \tag{50}$$

where Y_0 denotes the baseline prediction, $Y_{+20\%}$ and $Y_{-20\%}$ represent the predicted outputs obtained by increasing and decreasing the investigated parameter by 20%, respectively. A larger absolute value of SC indicates a stronger influence of the corresponding parameter on the model prediction.

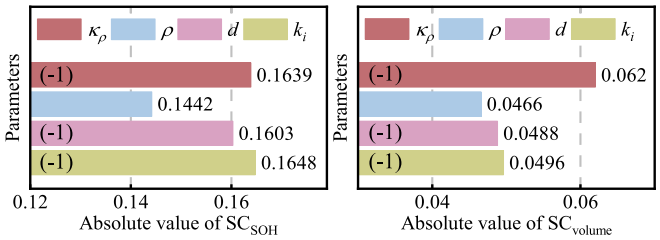


Fig. 15. Sensitivity analysis results of key transport parameters on model outputs after 300 cycles.

Fig. 15 indicates that the membrane hydraulic permeability and vanadium-ion diffusion coefficients exhibit the highest sensitivity among the investigated parameters. This can be attributed to their direct influence on water migration and ion crossover across the membrane, which are the primary driving forces of electrolyte imbalance and long-term capacity decay. In contrast, the effects of initial electrolyte viscosity are comparatively limited within the investigated uncertainty range.

Furthermore, although parameter perturbations affect the quantitative prediction results to some extent, the dominant degradation mechanism identified by the model remains unchanged. In all investigated cases, osmotic-pressure-driven water transport continues to be the primary contributor to long-term electrolyte volume imbalance. These findings demonstrate that the proposed model possesses reasonable robustness against uncertainties in key transport parameters.

5. Conclusions

This study presents a physics-based model developed from the principles of mass and charge conservation to accurately capture capacity decay and electrolyte migration in VRBs. Compared with state-of-the-art model, the model introduces incremental improvements by correcting the convection term in the vanadium ion concentration equations and the pressure difference term in the electrolyte volume equations. As a novel enhancement, it captures the dynamic behavior of proton migration during VRB operation. The model incorporates four critical factors: ion crossover and side reactions, main reaction, shunt current, and osmotic pressure, which collectively influence the volumes of positive and negative electrolytes. The model was validated through a 300-cycle charge-discharge experiment. Simulation results reveal that these four factors contribute to imbalances in vanadium ion concentrations and electrolyte volume, resulting in battery capacity fading. Osmotic pressure is identified as the dominant contributor to electrolyte imbalance. Furthermore, the model was extended to cells in different current densities and cell sizes. Results preliminary demonstrate that proposed model can reasonably capture the long-term degradation trends under different investigated operating conditions. This work provides useful mechanistic insights into electrolyte crossover-induced capacity fading in VRBs and establishes a theoretical foundation for future degradation analysis and operational optimization studies. Nevertheless, additional validation under stack-level configurations and broader practical operating conditions will be necessary in future work to further evaluate the engineering applicability of the proposed model.

Effects of migration and convection are important for accurate crossover modeling [45]. But the migration effects in the simulation of ion crossover are not considered in the work, and will be considered under certain operating conditions to further improve crossover accuracy in future work.

Although the proposed model demonstrates good predictive capability under these investigated conditions, additional validation under stack-level configurations and broader practical operating environments

will still be necessary in future work to further evaluate its engineering applicability and scalability.

CRediT authorship contribution statement

Shaojin Wang: Writing – original draft, Methodology. **Jinrui Tang:** Supervision, Software. **Binyu Xiong:** Writing – review & editing, Project administration, Funding acquisition. **Yang Li:** Writing – review & editing, Supervision. **Changjun Xie:** Validation, Methodology. **Feifei Dong:** Formal analysis, Data curation. **Xinan Zhang:** Validation, Supervision.

Declaration of competing interest

The authors declare that they have no known competing financial interests or personal relationships that could have appeared to influence the work reported in this paper.

Acknowledgments

This work is supported by the National Natural Science Foundation of China (No. 52177221).

Data availability

Data will be made available on request.

References

[1] Amini K, Shocron AN, Suss ME, Aziz MJ. Pathways to high-power-density redox flow batteries. ACS Energy Lett 2023;8:3526–35.
[2] Yuan T, Chen X, Zhao Y, Jiang Y, Li B, Zhao N, et al. Bridging the charge gap: Nb2CT /Nb2O5 schottky heterojunctions as electronic highways in vanadium redox flow battery. J Energy Chem 2026;113:771–9.
[3] Li H, Bin Kaleem M, Liu Z, Wu Y, Liu W, Huang Z. IoB: internet-of-batteries for electric vehicles–architectures, opportunities, and challenges. Green Energy Intell Transp 2023;2:100128.
[4] Yang Y, Wang X, Wang Y, Qiu G, Song Z, Xiong S. Functional nano-carbon layer decorated carbon felt electrode for vanadium redox flow batteries. J Energy Chem 2025;106:735–41.
[5] Wang S, Li Y, Li C, Lin X, Ma W, Tong N, et al. A systematic study of pipe and electrical connections for multi-stack vanadium redox flow battery modules considering electrolyte transport delays. Chem Eng J 2025;519:164929.
[6] Chen X, Li L, Jiang Y, Feng Z, Li Q, Jiang L, et al. Manipulating the local electronic structure microenvironment at the MXene interface to achieve efficient anode for vanadium redox flow battery. J Energy Chem 2025;104:118–26.
[7] Sun C, Chen J, Zhang H, Han X, Luo Q. Investigations on transfer of water and vanadium ions across nafion membrane in an operating vanadium redox flow battery. J Power Sources 2010;195:890–7.
[8] Xiong R, Xiong B, Zhang Q, Shi S, Su Y, Zhang D. Capacity fading model of vanadium redox flow battery considering water molecules migration. Int J Green Energy 2022;19:1613–22.
[9] Sun J, Li X, Xi X, Lai Q, Liu T, Zhang H. The transfer behavior of different ions across anion and cation exchange membranes under vanadium flow battery medium. J Power Sources 2014;271:1–7. https://doi.org/10.1016/j.jpowsour.2014.07.111.
[10] Song Y, Li X, Xiong J, Yang L, Pan G, Yan C, et al. Electrolyte transfer mechanism and optimization strategy for vanadium flow batteries adopting a nafion membrane. J Power Sources 2020;449:227503.
[11] Loktionov P, Pustovalova A, Pichugov R, Konev D, Antipov A. Quantifying effect of faradaic imbalance and crossover on capacity fade of vanadium redox flow battery. Electrochim Acta 2024;485:144047. https://doi.org/10.1016/j.electacta.2024.144047.
[12] Oh K, Moazzam M, Gwak G, Ju H. Water crossover phenomena in all-vanadium redox flow batteries. Electrochim Acta 2019;297:101–11. https://doi.org/10.1016/j.electacta.2018.11.151.
[13] Zou W-J, Kim Y-B, Jung S. Capacity fade prediction for vanadium redox flow batteries during long-term operations. Appl Energy 2024;356:122329.
[14] Shan J, Xiao D. Uncovering the effect of ion exchange membrane on capacity decay and efficiency for all-vanadium redox flow battery by modeling analysis. Int J Green Energy 2022;19:1367–74. https://doi.org/10.1080/15435075.2021.1997752.
[15] Chen H, Li X, Gao H, Liu J, Yan C, Tang A. Numerical modelling and in-depth analysis of multi-stack vanadium flow battery module incorporating transport delay. Appl Energy 2019;247:13–23.
[16] Chen H, Wang S, Gao H, Feng X, Yan C, Tang A. Analysis and optimization of module layout for multi-stack vanadium flow battery module. J Power Sources 2019;427:154–64.
[17] Zou W-J, Jung S. Asymmetric auto-rebalancing of electrolyte for high capacity retention and high energy efficiency of vanadium redox flow batteries. Appl Energy 2025;388:125663.
[18] Skyllas-Kazacos M, Goh L. Modeling of vanadium ion diffusion across the ion exchange membrane in the vanadium redox battery. J Membr Sci 2012;399–400:43–8. https://doi.org/10.1016/j.memsci.2012.01.024.
[19] Sukkar T, Skyllas-Kazacos M. Water transfer behaviour across cation exchange membranes in the vanadium redox battery. J Membr Sci 2003;222:235–47. https://doi.org/10.1016/S0376-7388(03)00309-0.
[20] Li Y, Sun L, Cao L, Bao J, Skyllas-Kazacos M. Dynamic model based membrane permeability estimation for online SOC imbalances monitoring of vanadium redox flow batteries. J Energy Storage 2021;39:102688.
[21] Li Y, Skyllas-Kazacos M, Bao J. A dynamic plug flow reactor model for a vanadium redox flow battery cell. J Power Sources 2016;311:57–67. https://doi.org/10.1016/j.jpowsour.2016.02.018.
[22] Xiong B, Li Y, Ding Y, Wang J, Wei Z, Zhao J, et al. Numerical analysis of vanadium redox flow batteries considering electrode deformation under various flow fields. J Power Sources 2023;564:232814.
[23] Xiong B, Zhao J, Su Y, Wei Z, Skyllas-Kazacos M. State of charge estimation of vanadium redox flow battery based on sliding mode observer and dynamic model including capacity fading factor. IEEE Trans Sustain Energy 2017;8:1658–67.
[24] Bogdanov S, Pugach M, Parsegov S, Vlasov V, Ibanez FM, Stevenson KJ, et al. Dynamic modeling of vanadium redox flow batteries: practical approaches, their applications and limitations. J Energy Storage 2023;57:106191.
[25] Xiong B, Zhao J, Tseng KJ, Skyllas-Kazacos M, Lim TM, Zhang Y. Thermal hydraulic behavior and efficiency analysis of an all-vanadium redox flow battery. J Power Sources 2013;242:314–24.
[26] Zheng Q, Zhang H, Xing F, Ma X, Li X, Ning G. A three-dimensional model for thermal analysis in a vanadium flow battery. Appl Energy 2014;113:1675–85. https://doi.org/10.1016/j.apenergy.2013.09.021.
[27] Wang S, Tang J, Xiong B, Fan J, Li Y, Chen Q, et al. Comparison of techniques based on frequency response analysis for state of health estimation in lithium-ion batteries. Energy 2024;304:132077.
[28] Li J, He S, Yang Q, Wei Z, Li Y, He H. A comprehensive review of second life batteries toward sustainable mechanisms: potential, challenges, and future prospects. IEEE Trans Transp Electrif 2023;9:4824–45.
[29] Ouyang T, Zhang M, Qin P, Tan X. Flow battery energy storage system for microgrid peak shaving based on predictive control algorithm. Appl Energy 2024;356:122448.
[30] Prieto-Díaz PA, Trovò A, Marini G, Rugna M, Vera M, Guarnieri M. Experiment-supported survey of inefficient electrolyte mixing and capacity loss in vanadium flow battery tanks. Chem Eng J 2024;492:152137.
[31] Pugach M, Kondratenko M, Briola S, Bischi A. Zero dimensional dynamic model of vanadium redox flow battery cell incorporating all modes of vanadium ions crossover. Appl Energy 2018;226:560–9. https://doi.org/10.1016/j.apenergy.2018.05.124.
[32] Wang H, Pourmousavi SA, Li Y, Soong WL, Zhang X, Xiong B. A new zero-dimensional dynamic model to study the capacity loss mechanism of vanadium redox flow batteries. J Power Sources 2024;603:234428. https://doi.org/10.1016/j.jpowsour.2024.234428.
[33] Xiong B, Dong S, Li Y, Tang J, Su Y, Gooi HB. Peak power estimation of vanadium redox flow batteries based on receding horizon control. IEEE J Emerg Sel Top Power Electron 2023;11:154–65.
[34] Li Y, Vilathgamuwa M, Choi SS, Xiong B, Tang J, Su Y, et al. Design of minimum cost degradation-conscious lithium-ion battery energy storage system to achieve renewable power dispatchability. Appl Energy 2020;260:114282.
[35] Xiong B, Ding Y, Zhang Q, Shi S, Zhang H, Su Y. Finite element-based analysis of composite serpentine flow channel 3D modeling of vanadium redox flow battery. Int J Green Energy 2022:1–8.
[36] Tang A, Bao J, Skyllas-Kazacos M. Dynamic modelling of the effects of ion diffusion and side reactions on the capacity loss for vanadium redox flow battery. J Power Sources 2011;196:10737–47.
[37] Xiong B, Tang J, Li Y, Zhou P, Zhang S, Zhang X, et al. A flow-rate-aware data-driven model of vanadium redox flow battery based on gated recurrent unit neural network. J Energy Storage 2023;74:109537.
[38] Pugach M, Bogdanov S, Vlasov V, Erofeeva V, Parsegov S. Identification of crossover flux in VRFB cells during battery cycling. J Power Sources 2024;610:234745. https://doi.org/10.1016/j.jpowsour.2024.234745.
[39] Xiong B, Tang J, Li Y, Xie C, Wang Z, Zhang X, et al. Design of a two-stage control strategy of vanadium redox flow battery energy storage systems for grid application. IEEE Trans Sustain Energy 2022;13:2079–91.
[40] Prieto-Díaz PA, Maurice AA, Vera M. Measuring density and viscosity of vanadium electrolytes: a database with multivariate polynomial fits. J Energy Storage 2024;94:112429. https://doi.org/10.1016/j.est.2024.112429.
[41] Ai F, Wang Z, Lai N-C, Zou Q, Liang Z, Lu Y-C. Heteropoly acid negolytes for high-power-density aqueous redox flow batteries at low temperatures. Nat Energy 2022;7:417–26.
[42] Wang S, Zhou Y, Li Y, Li C, Lin X, Zhang X, et al. Asymmetric variable flow-rate control enhances capacity and efficiency in vanadium redox flow batteries. J Energy Storage 2025;140:118954. https://doi.org/10.1016/j.est.2025.118954.
[43] Mohamed MR, Leung PK, Sulaiman MH. Performance characterization of a vanadium redox flow battery at different operating parameters under a

standardized test-bed system. Appl Energy 2015;137:402–12. https://doi.org/10.1016/j.apenergy.2014.10.042.
[44] Levanov AV, Isaikina Oya, Gurbanova UD, Lunin VV. Dissociation constants of perchloric and sulfuric acids in aqueous solution. J Phys Chem B 2018;122:6277–86.
[45] Chen Y, Bao J, Xu Z, Gao P, Yan L, Kim S, et al. A hybrid analytical and numerical model for cross-over and performance decay in a unit cell vanadium redox flow battery. J Power Sources 2023;578:233210. https://doi.org/10.1016/j.jpowsour.2023.233210.